Mechanical responses of a-axis GaN Nanowires under axial loads

R.J. Wang,[1] C.Y. Wang[1*], Y.T. Feng[1], Chun Tang[2]

1. Zienkiewicz Centre for Computational Engineering, College of Engineering, Swansea University, Bay Campus, Swansea, SA1 8EN, UK

2. Faulty of Civil Engineering and Mechanics, Jiangsu University, No. 301 Xuefu Road, Zhenjiang, Jiangsu, P.R. China 210013

Keywords: GaN Nanowires, Surface Elastic Properties, Size-effect, Fracture Behavior

Abstract Gallium Nitride (GaN) nanowires (NWs) hold technological significance as functional components in emergent nano-piezotronics. However, the examination of their mechanical responses, especially the mechanistic understanding of behavior beyond elasticity (at failure) remains limited due to the constraints of in-situ experimentation. We therefore performed molecular dynamics (MD) simulation on the mechanical behavior of $[1\bar{2}10]$-oriented GaN NWs subjected to tension or compression loading until failure. The mechanical properties and critical deformation processes are characterized in relation to NW size and loading conditions. Detailed examination reveals that the failure mechanisms are size-dependent and in here controlled by the dislocation mobility on shuffle-set pyramidal planes. The size dependence of the elastic behaviors is also examined in terms of the surface structure determined modification of Young's modulus. In addition, comparison with c-axis NWs is made to show how size-effect trends vary with the growth orientation of NWs.

Corresponding author: chengyuan.wang@swansea.ac.uk

1. Introduction

Gallium Nitride (GaN) is a versatile semi-conductor with high thermal stability, excellent electrical and tunable optical properties making it a highly desirable basis material for multifunctional device design. With the fabrication of near-pristine GaN nanostructures, particularly nanowires (NWs), it is possible to further enhance its electromechanical properties through size-effect and create a unique synergy between semiconducting and piezoelectric properties ideal for the emerging concept of nano-piezotronics [1–7]. As such, GaN NWs are considered as key functional components in future nano-actuators, generators and nanoelectromechanical systems (NEMSs) [8–13]. In this context, it is essential to understand the mechanical properties and behaviors of GaN NWs, especially at failure, as they delineate the reliability and robustness of the envisioned systems.

The majority of previous investigations on GaN NW mechanical responses have focused on characterizing the size-dependence of the elastic modulus and relating the elastic property alterations to the specific structures on free surfaces (or facets). For m-axis ($[10\bar{1}0]$ oriented triangular shaped) NWs, in situ electromechanical resonance and nano-indentation has been performed to characterize the size-effect on the elasticity [14,15]. Atomic force microscope was used to measure elastic modulus for the a-axis ($[1\bar{2}10]$ oriented triangular shaped) and c-axis ($[0001]$ oriented hexagonal shaped) NWs in three point bending tests [16,17]. Bernal *et.al.* [18] demonstrated (using combined in-situ MEMs tension test and MD simulations) that the elastic modulus increased with decreasing diameter for GaN NWs. The stiffening effect was attributed to the surface induced bond contraction strengthening similar to the mechanism achieved for Zinc Oxide NWs via MD studies [19]. However, discrepancy existed in the nature of the size-effect.

Initial investigation into GaN NW failure behavior was performed by Wang *et.al.* [20] via MD to characterize the tensile responses of all attainable growth orientations for thin sizes of 2-3 nm. Failure properties and mechanisms were found to be dependent on orientation. The brittle-to-ductile transition was observed in c-axis NWs between temperatures of 1500 K to 1800 K. A complementary study [21], by the same group further examined the orientation effect on axially compressed buckling and non-linear post-buckling behavior of the thin GaN NWs. More recently, Jung *et.al.* [22] performed MD simulation on c-axis NW behavior at the 2-5*nm* size range. An unanticipated wurtzite to tetragonal phase transition was observed previous to ultimate fracture and the size dependence of fracture stress is observed. Experimentally, Brown *et.al.* [23] performed in-situ MEMs tension test on c-axis GaN NWs where failure by transverse fracture is found. The fracture stress falls in the range of 4.5-7.5 *GPa* with unexpectedly high fracture strains of 1-4%. For a-axis GaN NWs, compression test was carried out by Huang *et.al.* [24] utilizing TEM-SPM indenter. The results demonstrate brittle failure where fracture stresses increased from 0.21 to 1.76 *GPa* as diameter decreased. It is observed that dislocation slip on the $\{10\bar{1}0\}$ planes (a major GaN slip system) occurred and initiated the fracture process.

Motivated by these pioneering studies, the present work aims to characterize the size-dependence of NW failure to further the mechanistic understanding of failure behaviors for GaN NWs (5-12.5*nm*) in the a-axis orientation. The analysis is based on MD simulations where both tensile and compressive loading is considered to observe possible asymmetry in the stress-strain relation and the deformation processes. The size-effect is characterized for critical properties and more significantly the deformation mechanisms underlining the failure behavior. Finally, size-effect origin is discussed through the relationship of structural features, particularly on surfaces, with the surface elastic modulus modification. Comparisons between the orientations are made to

underscore the prominent role of surface structure in the diverse mechanical properties observed. Herein, the atomistic simulation procedure and potential function used are discussed in Sec.2. The computational results and major issues are discussed in Sec. 3. The new findings are summarized in Sec.4.

2. Methodology

Based on experimentally observed stable structures of $[1\bar{2}10]$ oriented (a-axis) GaN NW, the model NWs hold triangular cross-sections with bounding facets formed by the $\{10\bar{1}1\}$ and $(000\bar{2})$ planes (Fig. 1) [18]. The characteristic size of these NWs is defined here by the cross-sectional width, b, (Fig. 1). To facilitate the suitable capture of size effect, the mechanical responses of GaN NWs sized 5 to 12.5 *nm* are examined through simulated axial loading. In so, the mechanical properties discussed here will imply the $[1\bar{2}10]$ or axial direction unless specified otherwise. Other NW dimensions are maintained at a constant ratio to b where the length, l, is set as 5b and the cross-sectional height, h, as ~1b (Fig. 1).

The atomistic simulation of NW uniaxial deformation are performed via molecular dynamics (MD) and molecular statics (MS) techniques utilizing the LAMMPS software package [25]. The interaction energy is modelled by a combination of the short-range Buckingham potential and long-range Coulombic forces. Ion polarizability is represented via a massless shell model applied to the nitrogen atoms [26]. The detailed form follows:

$$E = \sum_{i}\sum_{j>i} A \cdot exp(-r_{ij}/\rho) - C{r_{ij}}^{-6} + E_{long}(r_{ij})$$

Where r_{ij} is the distance between an atom pair and A, C, ρ are parameters for the pair-wise interactions. The employed values are from [26] and the r_{ij} cut-off is set at 10Å. The long-range electrostatic energy is computed via the damped-shift method detailed in [27]:

$$E_{long} = \sum_{i} \sum_{\substack{j>i \\ r_{ij}<r_c}} q_i\, q_j \left[\frac{erfc(\alpha r)}{r} - \frac{erfc(\alpha r_c)}{r_c} + \left(\frac{erfc(\alpha r_c)}{{r_c}^2} + \frac{2\alpha}{\sqrt{\pi}} \frac{exp(\alpha^2 {r_c}^2)}{r_c} \right) (r - r_c) \right]$$

where q_i and q_j are the partial charges; α is the damping coefficient and r_c the cut-off radius respectively, and the values of 0.33 and 8Å are selected based on consistency of the interaction energy, E, with the Ewald summation benchmark [27]. The validity of the Buckingham core-shell potential has been demonstrated through reproduction of elastic coefficients, phase transition prediction, native defect energy calculations and characterization of thermal-mechanical properties of c-axis GaN NWs [22,26]. It is noted that the Stillinger-Weber (SW) potential was employed in previous GaN NW studies, which is shown to be reliable for bulk properties, mechanical behaviors, melting behavior and brittle-to-ductile transition [20,28,29]. In spite of the fact that these potentials can appropriately model the nanoscale GaN in different contexts, the adequate reproduction of the unique relaxation features of GaN surface has only been explicitly demonstrated for the Buckingham potential [26,30]. Therefore, this potential is selected for GaN NWs where the fracture behavior can be sensitive to the free surface structure and properties.

The deformation of NWs from equilibrium to failure is conducted at room temperature through quasi-static tension and compression loading. Time integration is performed through the Verlet algorithm with timestep of 0.5 fs to ensure energy convergence. The NW sample is first relaxed via the conjugate gradient minimization method at 0*K*. The energy-minimized structured is then heated to 300*K* and thermalized using the Noose-Hoover thermostat in the NVT ensemble for at least 1 ns or until the NW axial stress fluctuation is minimized. Subsequently, tensile or compressive loading is applied at a strain rate of $5 \cdot 10^{-5}$/ps with temperature maintained by the NVT thermostat. Each displacement load consists of $\pm$0.1% strain increment and followed by a relaxation period of 20 ps. It is important to note that during tension, periodic boundary condition

is imposed along the $[1\bar{2}10]$ deformation direction to eliminate end effects. However, to prevent unphysical behaviors during compression, the ends of the NWs are fixed to simulate effects of impacting pistons.

For NW Young's modulus, Y_{nw}, and surface elasticity effect quantification, a MS procedure was adopted to eliminate distortions by thermal noise [31]. Here, displacement loading is applied at increments of $\pm 0.05\%$ and up to a total engineering strain of $\pm 2\%$. The NW structure is equilibrated at zero strain and during loading by the conjugate gradient method. Subsequently, the total energy of the NW and its component layers were computed by summing the constituent atomic energies. The axial stress of the NWs is computed via the arithmetic mean of virial stress [32], as follows:

$$E = \frac{1}{N}\sum_{i=1}^{N}\frac{1}{V_i}\left(m_i v_z^i v_z^i + \frac{1}{2}\sum_{\substack{j=1 \\ (j\neq i)}}^{N} F_z^{ij}(\varepsilon_z) r_z^{ij}(\varepsilon_z)\right)$$

Where V_i is the atomic volume and N is the number of atoms; v_z^i and F_z^{ij} is respectively the velocity and the interaction force component in the $[11\bar{2}0]$ direction for the i^{th} atom. The rendering of nanowire structures are produced via the OVITO visualization software. [33]

3. Results and discussion

3.1 Tensile Behavior and Properties

For axial tensile loads, the obtained stress-strain relation is plotted in Fig. 2 for four GaN NWs sized 5*nm*, 7.5*nm*, 10*nm* and 12.5*nm*. Across all sizes, the relation is linear at strain $\varepsilon \leq 2\%$. At higher strains, a variable gradient is apparent where the slope decreases with rising strain (i.e., strain softening effect). The limit of this non-linear region is marked by rapid stress decrease to

vanishing values characteristic of brittle fracture. Therefore, the fracture strength σ_f and strain ε_f of the a-axis NWs is defined by the maximum stress and associated strain. Evident from Fig. 2 the fracture strength and strain sensitivity to size variation differ markedly (inset details the respective relationships). The decrease in σ_f is the greatest for the thin NWs where σ_f significantly decreases from 23.30 to 20.46 *GPa* by ~5-8% when the size rises from 5 to 10*nm*. The change dramatically reduces to ~0.9% when size increases from 10 to 12.5*nm*, corresponding to a variation of σ_f from 20.46 to 20.26 *GPa*. Size effect is thusly achieved for the fracture strength of the a-axis GaN NW, which increases with the decrease of the size. In [20], 38 and 36*GPa* were obtained for 2.08 and 2.60 *nm* NW, which corroborates the trend achieved here. On the other hand, size effect is trivial for the fracture strain as evident in Fig. 2 where ε_f maintains a value of 10.1% ± 0.1% for all sizes considered. The size-dependent behavior of the fracture strength can be attributed to the axial stiffness increase with decreasing NW size. Evidently, as the fracture strain in Fig. 2 is approximately constant, the higher axial stiffness (i.e. Young's modulus) for smaller sizes ultimately produces a higher fracture strength. The exact relation of Young's modulus to size and discussion of the physical origins will be presented separately in a latter section.

With fracture properties of a-axis NW in tension the orientation influence on failure behavior can be observed through the comparison with the MD results for hexagonal c-axis NWs calculated via the same interaction potential [22]. For c-axis NWs it is found that σ_f decreases from 30.6 to 24.6 *GPa* (~20%) as the size increases from 2.26 to 4.85 *nm*. The trend is qualitatively similar to the one of the present work but the σ_f values are higher and its rate of change with size is substantially larger than those obtained for the a-axis NWs of larger sizes. On the other hand, similar to a-axis NWs, ε_f for c-axis also maintains a constant value of 16.9% ± 0.35%. This value is larger than 10.1% ± 0.1% of a-axis NWs which is mostly due to the phase transition observed

in these ultrathin c-axis NWs. The higher fracture strength, fracture strain and the more substantial size effect on the fracture strength, derives from multiple factors including the smaller sizes considered in [22] and lattice anisotropy. Nevertheless, the most fundamental factor in the orientation effect remains the specific facet structure and associated relaxation (discussed later in Sec.3) as the phase transition and eventual fracture of NWs are initiated from the free surfaces.

Indeed, the a-axis NW facets facilitates distinct failure mechanisms. Overall, two types of failure modes are observed in the tensile tests at 300*K*. The first is the shear failure for the 5*nm* NW characterized by extensive, dislocation initiated sliding on an inclined plane (Fig.3 a and b). Detailed examination in Fig. 3 c-d shows that a dislocation half-loop nucleates in the corner A atom chain (Fig. 1) and traverses the NW along a shuffle-set $(1\bar{2}1\bar{2})$ plane. The dislocation is of the $(a+c)$ type with likely slip vector of $\sim 1/3\langle 1\bar{2}13\rangle$ as proposed in [34]. Although dislocation slip occurs, the shear deformation is restricted within 3 to 4 adjacent $(1\bar{2}1\bar{2})$ planes and shrinking of the cross-section is minor, which is coherent with the overall brittle behavior. The second failure mode observed for sizes 7.5*nm* or larger is cleavage fracture primarily along the transverse $(1\bar{2}10)$ plane under the action of the maximum tensile stress (Fig. 4 a and b). The onset of fracture is marked by activation of two slip systems, likewise also from corner A, causing dislocation glide in short succession on intersecting slip planes, i.e. $(\bar{1}2\bar{1}\bar{2})$ and $(1\bar{2}1\bar{2})$. Fig. 4 c illustrates (along the wedge region) the slip introduced by the first dislocation in blue and the second group in yellow with the shear directions indicated by the accompanying arrows. Due to the large slip vector magnitude and the shuffle motion, within the vicinity of the glide paths intersection (site C) significant lattice distortions accumulate (Fig. 4 c). The stress concentration result in the formation of cavities or nano-cracks in the region (Fig. 4 d), which subsequently initiates cracking along a transverse $(1\bar{2}10)$ plane and propagates throughout the NW under the tensile stress.

As shown above, a transition from shearing to cleavage fracture with size increase has been observed for a-axis GaN NWs, which is similar to the transition found in MD simulated tensile tests of cylindrical Silicon NWs [35,36]. There, the authors demonstrated that the failure behavior of Si NWs, i.e., shearing or cleavage fracture, depends on whether crack propagation or dislocation nucleation at crack tip occurs first. In the present work, the fracture observed is always initiated by the dislocation nucleation on the surface and affects the eventual cracking within the GaN NW via intersecting slip. Concomitant, dislocation glide is observed to continue during cavity formation but cannot sweep the entire GaN NW before crack initiation. Based on these behaviors, it is the dynamics of the nucleated dislocations on the $(\bar{1}2\bar{1}\bar{2})$ and $(1\bar{2}1\bar{2})$ planes in accordance with GaN NW size that determines the fracture mechanisms of the NWs. Hence, a critical cross-sectional size for the transition of the fracture mechanisms is also found between 5 and 7.5*nm* at the applied strain rate.

3.2 Compressional Behavior and Properties

The mechanical responses during axial compression are studied for GaN NWs sized 5 and 10*nm*. The stress-strain relations are presented in Fig. 5 for both NWs and the characteristic stages of the deformation processes are respectively shown in Figs. 6 and 7.

Examining the 5*nm* NW, the initial behavior in Fig. 5 is nearly linear elastic with a constant slope, which concludes at point 1 associated with the maximum stress σ_c = 27.70 *GPa* and strain ε_c = 5.7% and followed by a sharp stress decline. These results contrast with [21] where 2.6 nm NW at the same l/h exhibited critical stress/strain of 14 GPa and ~8.3%. (The difference likely arises from the variation in elastic constant as well as surface effect produced by the interatomic potentials.) This precipitous fall is instigated by the buckling of NW against the $(\bar{1}011)$ plane as shown in Fig. 6a, which reflects the overall structural instability without any prior local defect nucleation

observed. After the onset of the buckling, transverse or bending deflection in the $[\bar{1}011]$ direction increases slightly with rising axial compression. At the same time, twinning partial dislocations nucleate from the NW midsection where buckling induced local compressive stresses are the highest and glide along a shuffle-set $(1\bar{2}12)$ plane. Fig. 6b shows the structural and morphological changes when reaching point 2 of Fig. 5. As observed in Fig. 6c, such a twinning dislocation starts from the pairs of 10-atom rings defect on the $(10\bar{1}1)$ facet, which are formed by surface bond cleavage as the corner A atom chain buckles inward during the overall NW instability. Further increasing the strain past ε_c = 5.7% leads to nearly linear increase of stress (Fig. 5) associated with the growth of the twinned region. After reaching the local maximum at point 3 in Fig. 5 the stress decreased with rising strain. In this process, the NW experiences an increasing transverse deflection in the $[0001]$ direction, which finally results in fracture at the side of bending induced tension. These features are shown in Fig. 6d which is captured at point 4 (ε = 16%) in Fig. 5.

For the NW of size 10*nm*, the overall stress-strain relation remains qualitatively similar to that obtained for the smaller sample. Nevertheless, further examination shows that the size difference once again lead to different post-buckling deformation processes. Herein, buckling against the $(\bar{1}011)$ plane is again observed for the 10*nm* NW and the associated critical buckling stress σ_{cr} and strain ε_{cr} are 30.06 *GPa* and 6.5%, respectively. From Fig. 5, this is a sizeable increase, respectively, of 9% and 14% relative to the values found for the 5*nm* NW. Such σ_{cr} and ε_{cr} increments with larger size can be understood as a result of the competition between the stiffening effect of the larger area moment of inertia and the lower Young's modulus of the larger size NW.

Similar to the 5*nm* NW, following the onset of buckling a twinning partial dislocation (Fig. 7a site A) nucleates on the $(10\bar{1}1)$ facet and glides on a $(1\bar{2}12)$ plane. However, due to the larger

cross sectional size and the higher critical buckling load, before it can sweep through the entire cross section, the second partial dislocation nucleates (Fig. 7a site B) and glides on an intersecting $(\bar{1}2\bar{1}2)$ plane. Although the initial intersecting partial dislocation glides do not mutually impede, the subsequent deformation twinning along generated stacking faults A and B is strongly inhibited by the twin intersection. Thus, evident in Fig. 7 b, only very thin (2-3 lattice layers) twinned regions are formed along the stacking faults. This is likely attributable to the opposing twinning shears, which inhibits the further propagation of the respective shear strains through the intersection region (Fig. 7 b site C). Combined with the proximity of the intersection region and nucleation sites, twin growth by successive partial dislocation glide on adjacent $(\bar{1}2\bar{1}2)$ planes cannot be completed as the glide motions are obstructed near site C (Fig. 7 c). This finally suppresses the rapid advancement of the entire twin boundary.

In the high strain rate and low temperature regime of the current study, twinning in general is common for metallic systems in which the twinning via the $\{1\bar{2}12\}\langle 1\bar{2}13\rangle$ system is well-known in compression of hexagonal-close-packed metals [37,38]. Twinning dominated deformation in semiconductors has also been reported for bulk material [39–41] and microstructure [42]. Nevertheless, twinning on GaN pyramidal planes is unexpected as the indentation of mesoscale a-axis GaN NWs by Huang *et.al.* [24] mainly observes dislocation slip on the $\{10\bar{1}0\}$ and $(01\bar{1}\bar{1})$ prismatic planes. Indeed, as shown in [34], the generalized stacking fault energy (GSFE) is relatively high on both the glide and shuffle-set pyramidal planes. Thus, the twinning achieved on GaN pyramidal planes could result from the fact that, under high compressive stress, the preferred slip system can shift in pristine nanostructures due to the higher tolerance of inter-planar distance reduction. For instance, it has been found for Si NWs in [37] that, a transition from the commonly observed $\{111\}$ slip planes is driven by the dramatic GSFE

reduction for the unconventional $\langle 0\bar{1}1\rangle\{011\}$ slip system when compressed. Another vital factor to consider is that the deformation mechanisms are dominantly surface driven. Therefore, the synthesis specific defects and environment dependent microstructures of experimental NW facets become pivotal. For Si NWs, the activated slip plane is shown to strongly prefer planes directly intersecting the existing surface steps [43]. It is also well known that semi-conductor nanostructures are often coated by a thin amorphous or oxide surface layers [44,45] and that enviromental factors such as moisture content will modify the surface lattice structure as exemplifed in ZnO [46]. As such, since the present facets have idealized smoothness and factoring in the existence of planar defects in the NWs of [24], the difference in the preferred slip system activated and to an extent the overall compression deformation mechanism can be rationalized as compared to experimental findings.

It is worth mentioning that in previous MD study [21] a-axis NWs ($l/h > 6$ and $d = 2.6$nm) failed in beam-like buckling due to axial compression. The dislocation nucleation and twinning deformation found in the present work was not observed. Normally, slender structures, e.g. $l/h > 10$, buckles as an Euler beam (verified in our simulation but not shown here) and stocky structure, e.g. $l/d < 3$, fails by material fracture. For intermediate structure, e.g. $l/h \sim 5$, as shown in the present study, both failure modes are clearly observable. The beam-like buckling achieved at $l/h > 6$ shows that the long NWs is defined by $l/h > 6$ in [21] which is smaller than the corresponding value around 10 found in this work. Such difference can be attributable to the different cross-sectional sizes and/or interatomic potentials considered in the two studies.

3.3 Orientation Effect on Size Dependent Young's Modulus

As observed from the tensile stress-strain relations, failure properties size-dependence is a direct result of the higher Young's modulus in smaller NWs. Therefore, its physical origins can be established through an examination of size-effect on elastic behavior. To this end, the overall Young's modulus of the NWs, Y_{nw}, is computed in the following procedure. The total energy (E_{Total}) to axial strain (ε) relation is first plotted and its functional form is established by polynomial fitting. Then, Y_{nw} and Y_i^l are evaluated for each NW size by taking the second derivative of E_{Total} with respect to ε:

$$Y = \frac{1}{V_0}\left(\frac{\partial^2 E_{total}}{\partial \varepsilon^2}\right)_{\varepsilon=0} \qquad (1)$$

where V_0 denotes the nominal volume of the initial energy minimized NW structure. For V_0 evaluations, significant uncertainties exist due to the ambiguity in measuring characteristic sizes of low-dimensional structures. As shown in our previous study [47], different size definitions may lead to a reversed trend of the overall elastic modulus of GaN NWs. To ensure the selected characteristic size (*i.e.* cross sectional width, b) can be used to properly characterize Y_{nw}, an effective axial elastic modulus (S_p) defined in Eq.2 is also computed for the NW (S_{nw}) and its component layers (S_l^i). This equivalent elastic modulus is independent of the effective volume and thus, can be used as a reference to provide consistency in the selected effective width and associated Young's modulus.

$$S_p = \frac{1}{N_d}\left(\frac{\partial^2 E_{total}}{\partial \varepsilon^2}\right)_{\varepsilon=0} \qquad (2)$$

Here, as the stoichiometric ratio is maintained within each NW or its component layers, E_{Total} in Eq. 2 is normalized by N_d, the number of Ga-N dimer or formula unit, instead of V_o, to give the average energy per dimer (E_p) of an NW or its component layers. The bulk value normalized NW

Young's Modulus Y_{nw}/Y_{bulk} and elastic modulus S_{nw}/S_{bulk} are presented in Fig.8 for each NW size. Excellent coherence (relatively difference of < 0.56%) is observed between the two curves demonstrating that the selected effective cross-sectional width is able to appropriately reflect the underline physical behavior. Therefore, evident in Fig. 7, all Y_{nw} are enhanced versus Y_{bulk} of 294.18 *GPa* and a stiffening Y_{nw} size effect trend is predicted, where Y_{nw}/Y_{bulk} rises from 1.040 to 1.095 as the size decreases from 12.5 to 5*nm*. Similar trend is observed in MD results of [18] where increase of ~290 to 310 GPa occurs when the size of the NWs decreases from 20 to 5 nm and accompanying experimental measurement of 276 ± 13GPa (near bulk value) is obtained at the cross-sectional size of 44nm.

To provide insight into the obtained trend, radial distributions of S_p defined in Eq.2 are constructed by calculating S_p of each layer (S_l^i, i = 1 to n) of the NWs. From Fig. 9, a dramatic increase of the surface moduli S_l^n of ~19% from S_{bulk} is exhibited by all sizes considered while S_l^i (i =1,2,..n-1) of inner layers decreases monotonically by 0.1 to 2.7% relative to S_{bulk}. This distribution of the elastic modulus is found to be qualitatively similar to the one obtained for ZnO NWs [48]. Specifically, the type of size-dependence of Y_{nw} for GaN NW originates from the net effect of (1) a dominant surface elasticity effect arising from the combined bond-contraction strengthening and bond-loss softening, and (2) the minor effect of the interior non-linearity [49]. Since surface modulus is significantly elevated for a-axis GaN NWs, a corresponding stiffening Y_{nw} size-dependence is achieved. The size-dependent elasticity is also observed in c-axis GaN NWs [18], which is again controlled by the surface effects. However, the obtained surface modulus (S_l^n) [47] is lower than the corresponding bulk value due to the bond-loss at the surface. This low surface modulus results in a strong softening effect on the overall Young's modulus where Y_{nw} decrease with the decreasing size. This trend is opposite to the one obtained for a-axis GaN NWs.

Indeed, this observation can be corroborated by the $\sigma_{\mathrm{WZ}\rightarrow\mathrm{TS}}$ size-dependence detailed in [22]. We note that this trend is not realized in the σ_f values of c-axis NWs referenced in section 3.1 because σ_f is measured post the wurtzite-tetragonal phase transition.

Such difference across the orientations can be understood from the degree of bond alignment to the axial loading direction and the amount of surface structure relaxation on the $[0001]$ c-axis NWs with $\{1010\}$ facets, and $[1\bar{2}10]$ a-axis NWs with $\{10\bar{1}1\}$ and $(000\bar{2})$ facets. For simplicity of argument, we examine a short-range surface structure consisting of two adjacent Ga-N dimers and its nearest neighbors. On $\{1010\}$ surfaces this structure contains two bonds ($B_{\parallel}^{c}$) in parallel and six at ~70$^{\mathrm{O}}$ to the $[0001]$ axial direction, whereas on $\{10\bar{1}1\}$ or $(000\bar{2})$ facets the opposite occurs where six bonds ($B_{\parallel}^{a}$) are much more aligned (~20$^{\mathrm{O}}$) with and two perpendicular to the $[1\bar{2}10]$ axial direction. The amount of contraction found in $B_{\parallel}^{c}$ and $B_{\parallel}^{a}$ is comparable at around 4-5% and can be expected to strengthen here similarly. Thus, the bond contraction strengthening effect is overall stronger in the axial direction of $[1\bar{2}10]$ a-axis NWs whereas the softening effect due to bond loss is much more dominant in the $[0001]$ c-axis NWs leading to the observed elasticity variation with NW faceting or orientation.

Although the dependence of surface elastic modulus on facet structural relaxation is inherent to nanostructures, its impact on the elasticity size-effect trend varies across systems. As demonstrated for Copper NWs, the interior non-linearity is instead the principle effect [50] and simple accounting of surface relaxation is insufficient to qualify the size-effect. This change in mechanism likely reflects the different amount of structural relaxation allowed by the metallic bonds and localized covalent bonds in semi-conductors.

4. Conclusions

MD simulations were performed to study the mechanical behaviors of *a*-axis GaN NWs (the cross-sectional < 12.5*nm*) subjected to axial loading. Attempts were made to explore the size-dependence of the elasticity, study the fracture mechanisms and the associated properties, and understand the distinctive features based on the surface elasticity and dislocation mobility.

In tensile tests, brittle fracture is observed for a-axis GaN NWs, where the fracture strain remains nearly a constant independent of the NW size but the fracture strength increases with the decreasing NW size due to the surface elasticity effect. Herein, dislocation initiated shearing failure is found in ultrathin NWs (the size < 5*nm*) on the $\{1\bar{2}1\bar{2}\}$ pyramidal planes. The cleavage fracture occurs for larger NWs (the size > 7.5*nm*), where dislocations nucleate on intersecting slip planes, i.e., $(1\bar{2}1\bar{2})$ and $(\bar{1}2\bar{1}\bar{2})$, and yields by cleavage along a transverse $(1\bar{2}10)$ plane. The NW size and dynamics of the dislocations/cracks are found to be the key factors to determine the fracture mechanisms.

In the compression of the NWs, buckling is observed as the first failure mode of the NWs where the critical buckling stress and strain increases with the increasing size of the NWs. Post-buckling deformation of ultrathin NWs occurs through defect assisted deformation twinning via the $\{1\bar{2}12\}\langle11\bar{2}3\rangle$ system, and results in tension fracture adjacent to the coherent twin boundaries where bend stresses are most concentrated. Deformation twinning also occurs for larger NWs but is inhibited by the intersection of twinned regions. Overall, the results highlight the asymmetry in behavior between tension and compression conventionally seen due to size-confinement.

Finally, MS calculations show that the Young modulus of a-axis GaN NWs increased significantly with decreasing the cross sectional size. The physical origin of the size dependence is the surface stiffening effect due to bond contraction on the $\{10\bar{1}1\}$ facets. This is in contrast to

the surface softening effect originating from the bond loss of the {1010} facets of c-axis GaN NWs [47]. Thus, different (or even opposite) effects of surface structure and the resulted trend of the size dependent Young's modulus and failure strength can be achieved for GaN NWs depending on the growth orientation of the NWs.

Figures

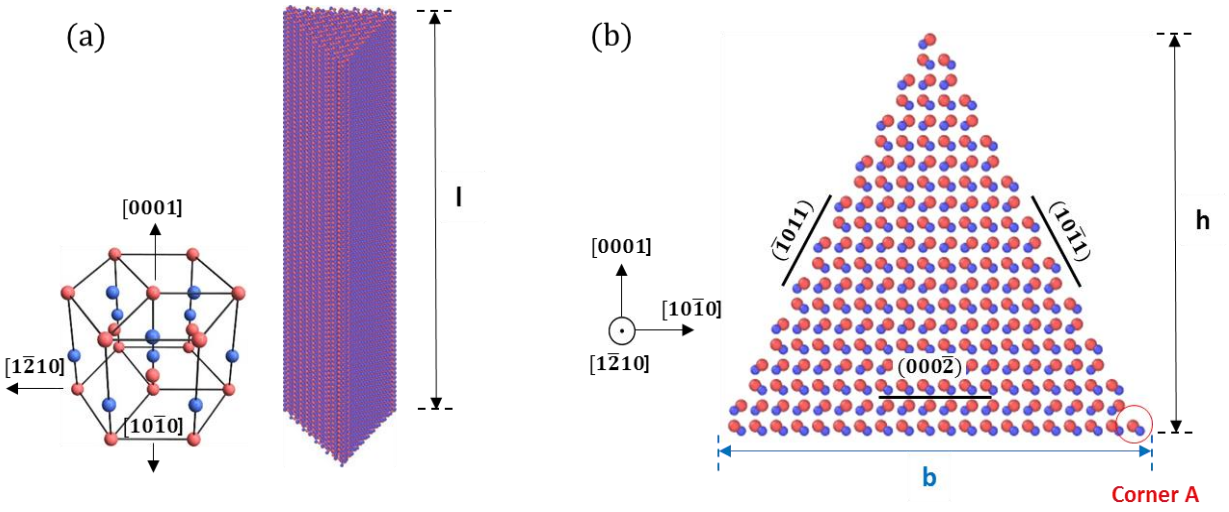

Figure 1. The structure of triangular a-axis GaN nanowire (a) oblique view of nanowire and wurtzite unit cell. l indicates the length of the nanowire (b) atomistic structure of nanowire cross-section. The growth orientation is $[1\bar{2}10]$ and the surrounding facets are $(\bar{1}011)$, $(10\bar{1}1)$, and $(000\bar{2})$ planes. b is the nanowire width, the characteristic nanowire dimension, and h is the cross-sectional height of the nanowire. Corner A denotes the surface atomic chain at the intersection of $(10\bar{1}1)$ and $(000\bar{2})$

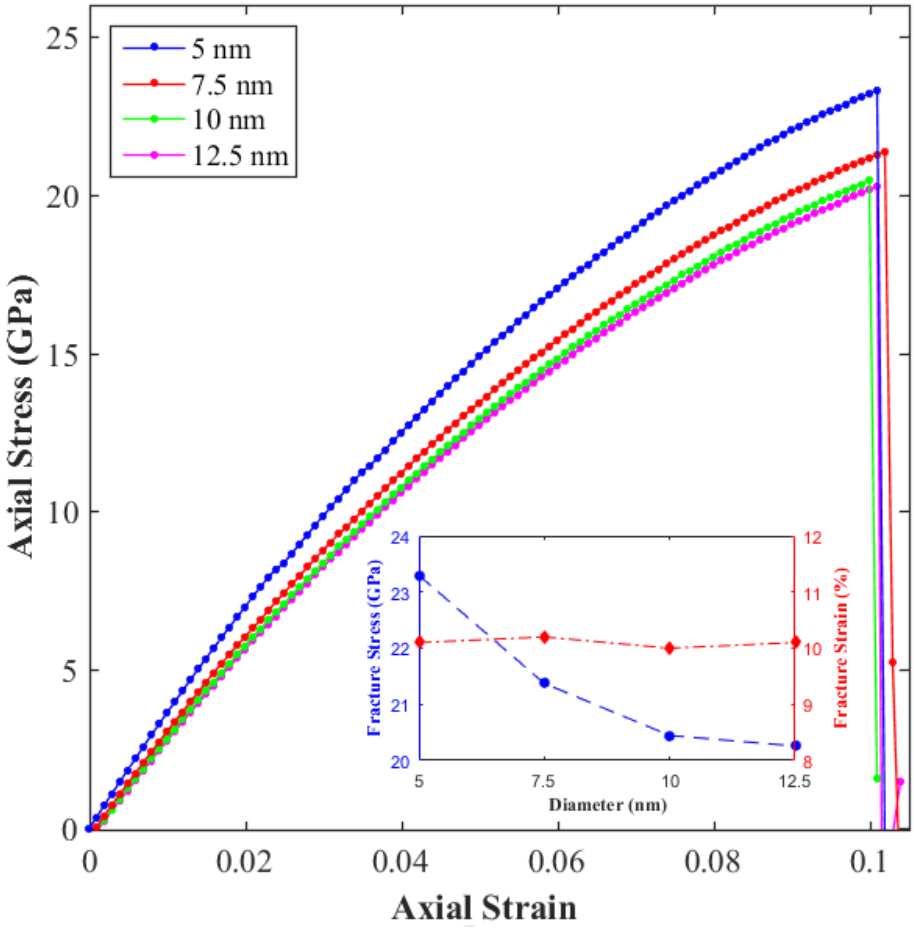

Figure 2. The stress-strain relationship of a-axis nanowires (5-12.5*nm*) under axial tension at 300*K*. Inset shows, respectively, the fracture stress (blue) and fracture strain (red) variation with characteristic nanowire size.

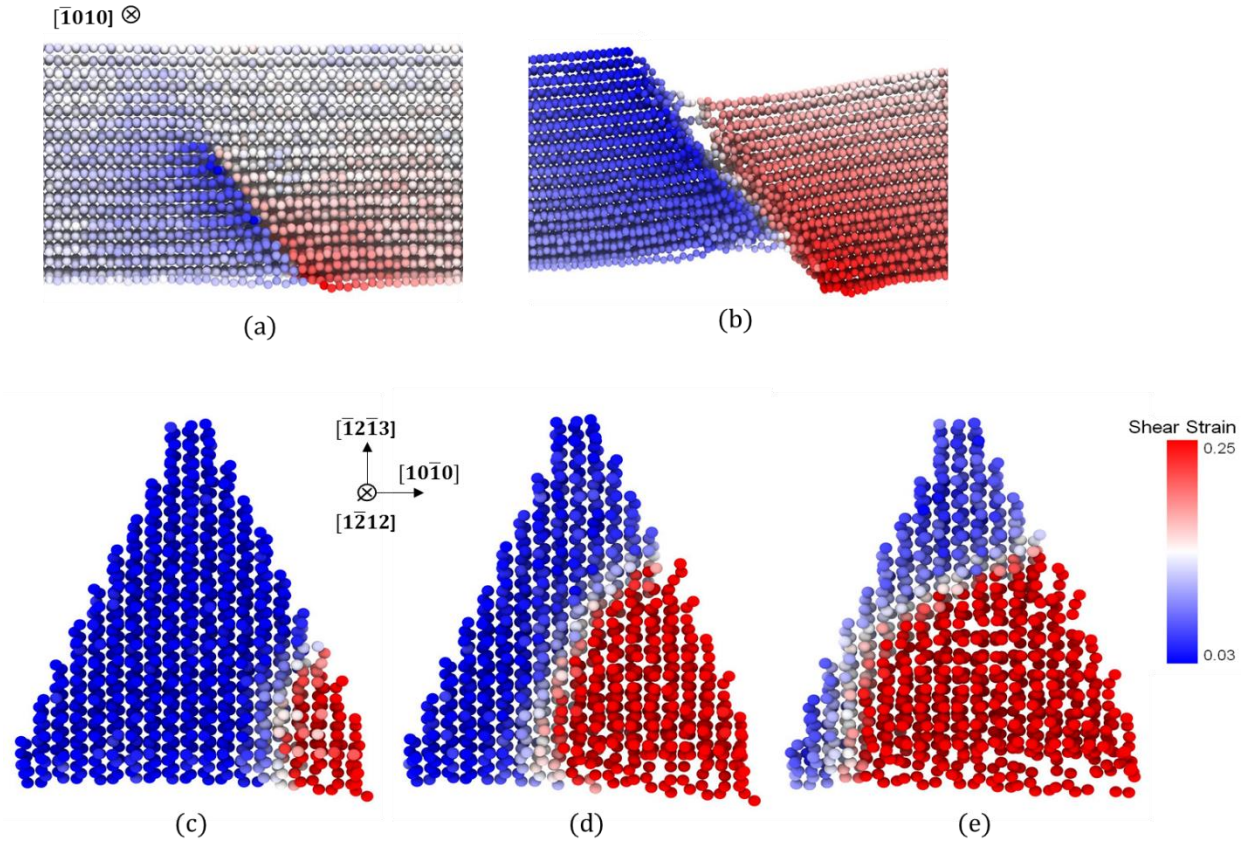

Figure 3. Structural deformation of *5nm* nanowire in tension at 300*K*. Viewed along the $[\bar{1}010]$ direction (a) dislocation half-loop nucleation and glide from corner A atomic chain. (b) Fracture of nanowire from dislocation initiated structural shearing. Viewed perpendicular to the $(1\bar{2}12)$ plane (c-e) dislocation loop propagation across the nanowire along the $(1\bar{2}12)$ plane with $[1\bar{2}13]$ slip direction and colored by the local shear strain.

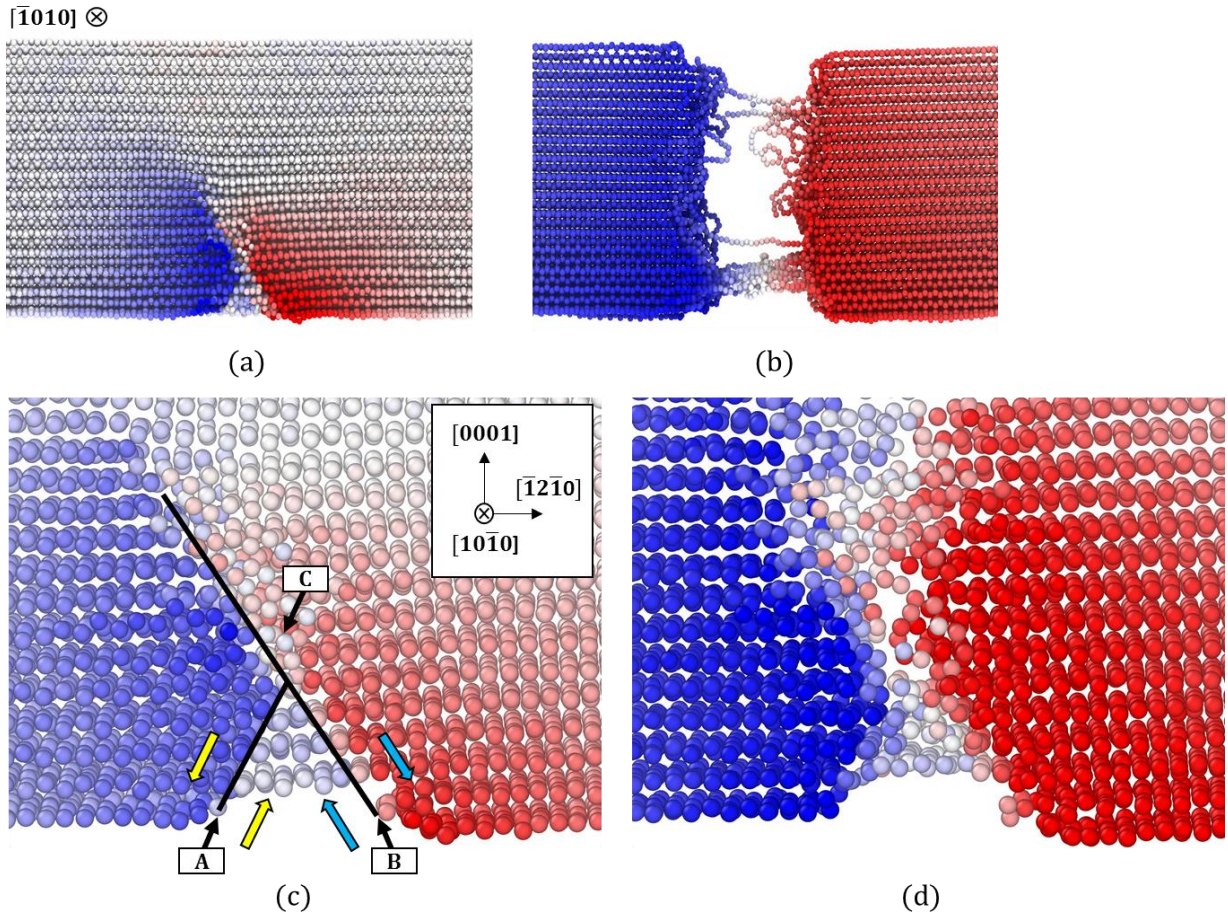

Figure 4. Structural deformation of 7.5*nm* nanowire in tension at 300*K*. Viewed along the $[\bar{1}010]$ direction and colored by displacement magnitude in the $[1\bar{2}10]$ direction. (a) Dislocation half-loop nucleation and glide from corner A atomic chain on two intersecting $\{1\bar{2}12\}\langle 1\bar{2}13\rangle$ slip system. (b) Cleavage fracture of nanowire along a $(1\bar{2}10)$ plane. The formation of highly distorted lattice around point C from intersecting slip of the two dislocations (c) and eventual cracking from point C (d). In (c) point B and A indicates the dislocation nucleation sites, where the first dislocation is nucleated at B. The blue and yellow arrows indicate the shear enacted on the lattice.

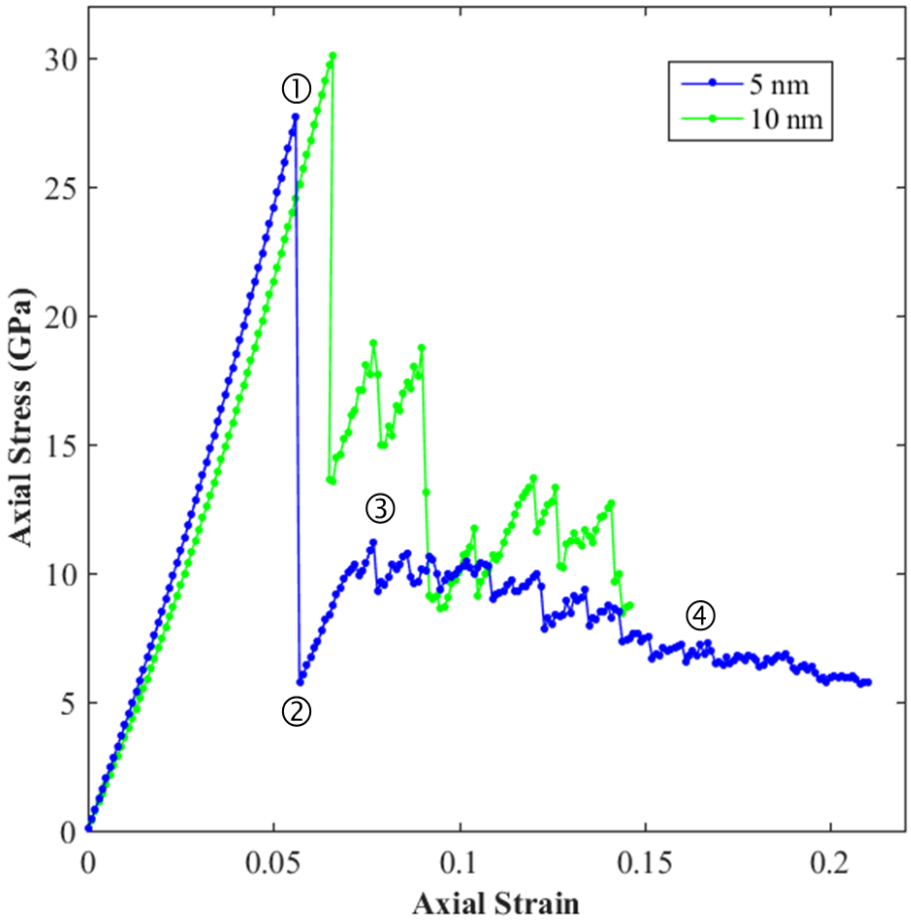

Figure 5. The stress-strain relationship of a-axis nanowires (5 and 10*nm*) under axial compression at 300 *K*.

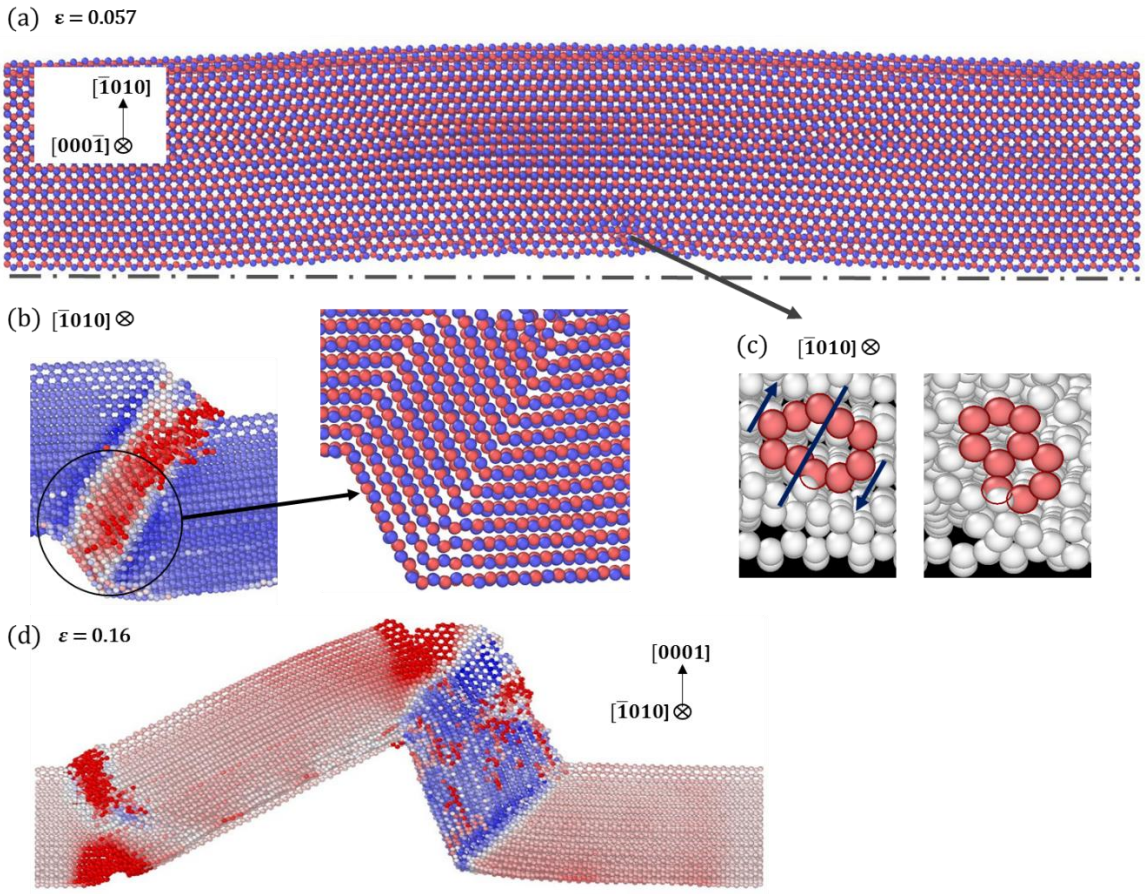

Figure 6. Compression deformation of 5*nm* nanowire at 300*K* viewed along different planes. (a) Buckling of nanowire (ε = 0.057), deflectioin in the $[\bar{1}010]$ direction. (b) Deformation twinning of nanowire along $(\bar{1}2\bar{1}2)$ twin plane. (c) The nucleation of twinning dislocation along a $(\bar{1}2\bar{1}2)$ plane from the 10-atom ring defect on the $(10\bar{1}1)$ facet. (d) Nanowire fracture from twin growth and resultant structural bending highlight in red (ε = 0.16).

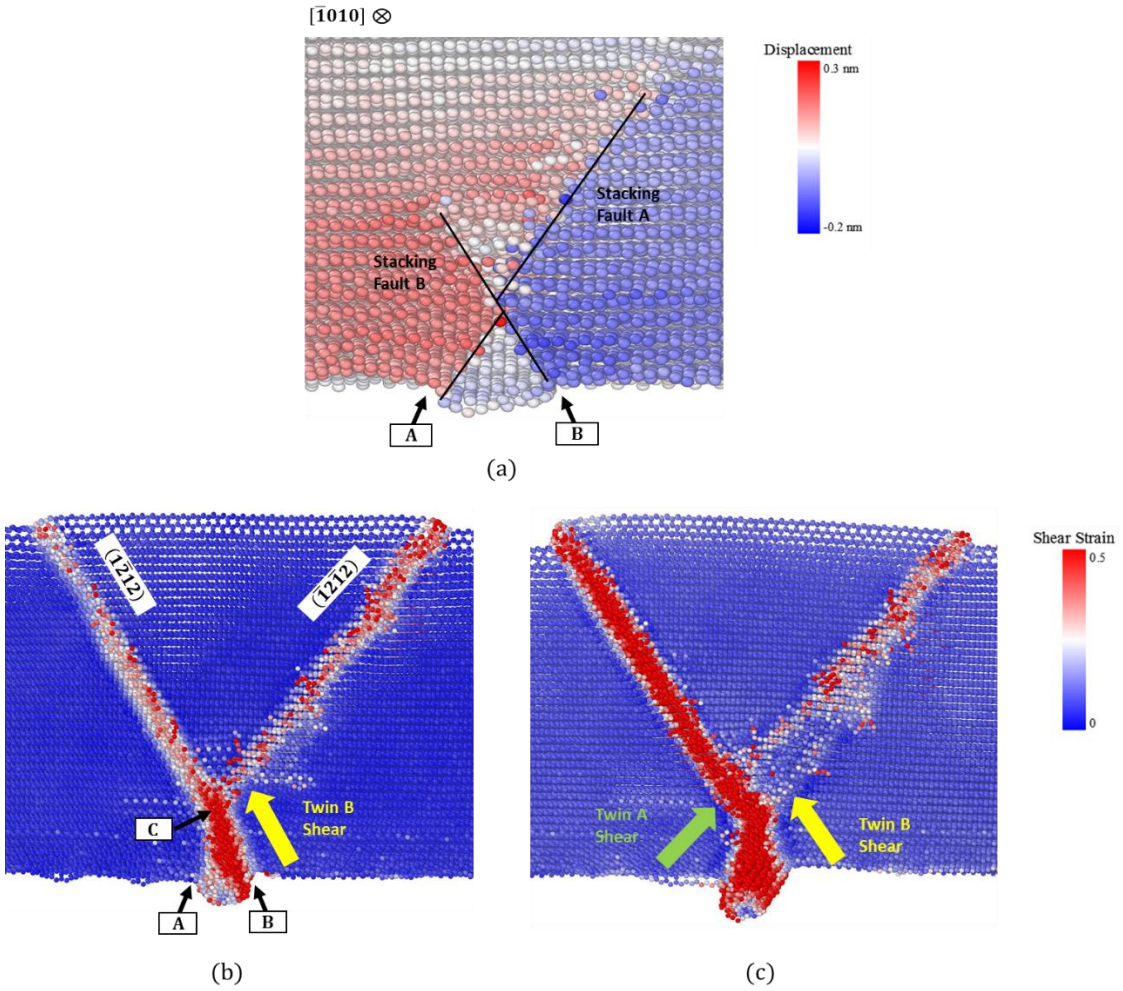

Figure 7. Compression deformation of 10*nm* nanowire at 300*K* viewed along the $[\bar{1}010]$ direction. Color map indicates $[1\bar{2}10]$ atomic displacement in (a) and shear strain in (b-c). (a) Nucleation of two twinning dislocations and their glide on intersecting $\{1\bar{2}12\}$ planes. Point A and B identifies the twinning partial dislocation nucleation sites and C the intersection region of the two twinning systems. (b) Two thin layers of twinned crystal (red) form along the stacking faults created by the initial dislocation glide (c) The twin intersection opposes proper twinning dislocation glide on adjacent $\{1\bar{2}12\}$ planes. Twin growth is severely restricted and lattice distortion accrue eventually released by structural sliding and further dislocation nucleation on other slip planes.

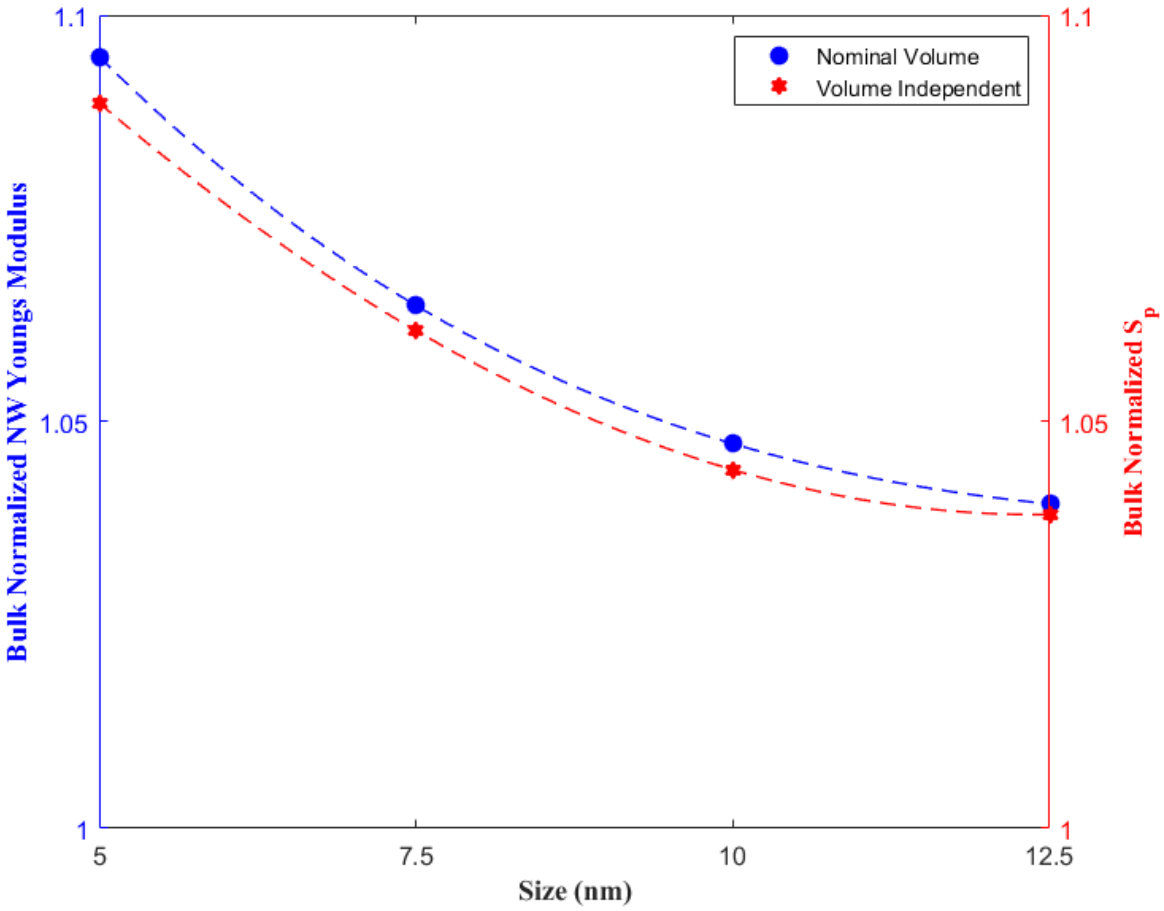

Figure 8. The bulk value normalized Young's modulus (blue) and elastic modulus S_p (red) in the nanowire axial direction ie. $[1\bar{2}10]$ for all nanowire sizes examined.

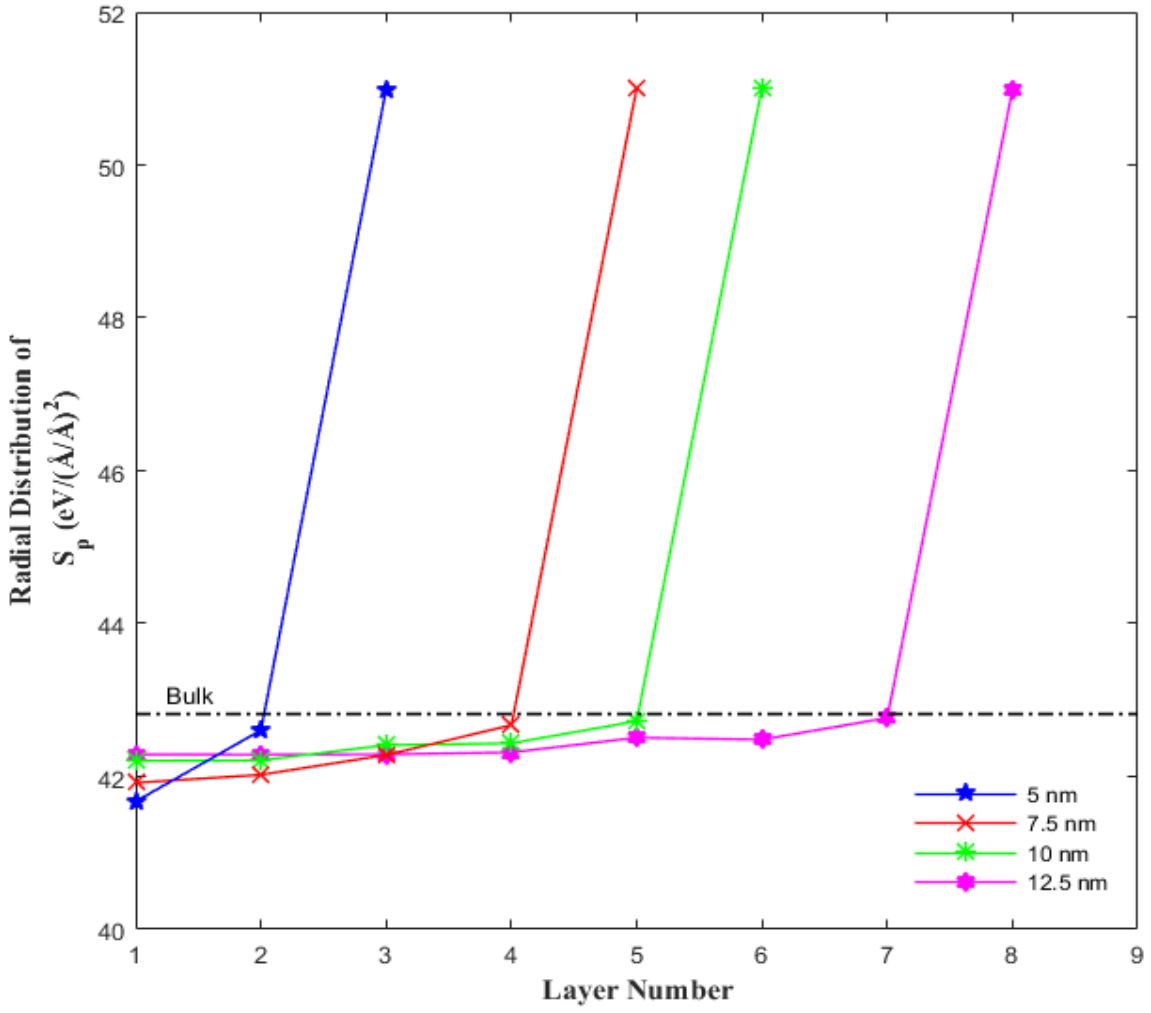

Figure 9. The axial elastic modulus (S_p) radial distribution for all nanowire sizes examined. The dashed line marks the corresponding bulk value.

References

[1] Cheng G S, Zhang L D, Zhu Y, Fei G T, Li L, Mo C M and Mao Y Q 1999 Large-scale synthesis of single crystalline gallium nitride nanowires *Appl. Phys. Lett.* **75** 2455–7

[2] Goldberger J, He R, Zhang Y, Lee S, Yan H, Choi H J and Yang P 2003 Single-crystal gallium nitride nanotubes *Nature* **422** 599–602

[3] Hersee S D, Sun X and Wang X 2006 The controlled growth of GaN nanowires *Nano Lett.* **6** 1808–11

[4] Tsivion D, Schvartzman M, Popovitz-Biro R, von Huth P and Joselevich E 2011 Guided Growth of Millimeter-Long Horizontal Nanowires with Controlled Orientations *Science (80-.).* **333** 1003–7

[5] Agrawal R and Espinosa H D 2011 Giant piezoelectric size effects in zinc oxide and gallium nitride nanowires. A first principles investigation *Nano Lett.* **11** 786–90

[6] Espinosa H D, Bernal R a. and Minary-Jolandan M 2012 A Review of Mechanical and Electromechanical Properties of Piezoelectric Nanowires *Adv. Mater.* **24** 4656–75

[7] Wang Z L and Wu W 2014 Piezotronics and piezo-phototronics: Fundamentals and applications *Natl. Sci. Rev.* **1** 62–90

[8] Jamond N, Chrétien P, Houzé F, Lu L, Largeau L, Maugain O, Travers L, Harmand J C, Glas F, Lefeuvre E, Tchernycheva M and Gogneau N 2016 Piezo-generator integrating a vertical array of GaN nanowires *Nanotechnology* **27** 1–22

[9] Johnson J C, Choi H-J, Knutsen K P, Schaller R D, Yang P and Saykally R J 2002 Single gallium nitride nanowire lasers *Nat. Mater.* **1** 106–10

[10] Wright J B, Campione S, Liu S, Martinez J A, Xu H, Luk T S, Li Q, Wang G T, Swartzentruber B S, Lester L F and Brener I 2014 Distributed feedback gallium nitride nanowire lasers *Appl. Phys. Lett.* **104** 41107

[11] Chen C Y, Zhu G, Hu Y, Yu J W, Song J, Cheng K Y, Peng L H, Chou L J and Wang Z L 2012 Gallium nitride nanowire based nanogenerators and light-emitting diodes *ACS Nano* **6** 5687–92

[12] Huang Y, Duan X, Cui Y and Lieber C M 2002 Gallium Nitride Nanowire Nanodevices *Nano Lett.* **2** 101–4

[13] Tanner S M, Gray J M, Rogers C T, Bertness K A and Sanford N A 2007 High- Q GaN nanowire resonators and oscillators *Appl. Phys. Lett.* **91** 203117

[14] Nam C-Y, Jaroenapibal P, Tham D, Luzzi D E, Evoy S and Fischer J E 2006 Diameter-dependent electromechanical properties of GaN nanowires. *Nano Lett.* **6** 153–8

[15] Feng G, Nix W D, Yoon Y and Lee C J 2006 A study of the mechanical properties of nanowires using nanoindentation *J. Appl. Phys.* **99** 76102

[16] Ni H, Li X, Cheng G and Klie R 2006 Elastic modulus of single-crystal GaN nanowires *J.*

Mater. Res. **21** 2882–7

[17] Chen Y, Stevenson I, Pouy R, Wang L, McIlroy D N, Pounds T, Grant Norton M and Eric Aston D 2007 Mechanical elasticity of vapour-liquid-solid grown GaN nanowires *Nanotechnology* **18** 135708

[18] Bernal R A, Agrawal R, Peng B, Bertness K A, Sanford N A, Davydov A V. and Espinosa H D 2011 Effect of growth orientation and diameter on the elasticity of GaN nanowires. A combined in situ TEM and atomistic modeling investigation *Nano Lett.* **11** 548–55

[19] Agrawal R, Peng B, Gdoutos E E and Espinosa H D 2008 Elasticity size effects in ZnO nanowires-A combined experimental- computational approach *Nano Lett.* **8** 3668–74

[20] Wang Z, Zu X, Yang L, Gao F and Weber W J 2007 Atomistic simulations of the size, orientation, and temperature dependence of tensile behavior in GaN nanowires *Phys. Rev. B* **76** 45310

[21] Wang Z, Zu X, Yang L, Gao F and Weber W J 2008 Molecular dynamics simulation on the buckling behavior of GaN nanowires under uniaxial compression *Phys. E* **40** 561–6

[22] Jung K, Cho M and Zhou M 2012 Thermal and mechanical response of [0001]-oriented GaN nanowires during tensile loading and unloading *J. Appl. Phys.* **112** 83522

[23] Brown J J, Baca A I, Bertness K A, Dikin D A, Ruoff R S and Bright V M 2011 Tensile measurement of single crystal gallium nitride nanowires on MEMS test stages *Sensors Actuators, A Phys.* **166** 177–86

[24] Huang J Y, Zheng H, Mao S X, Li Q and Wang G T 2011 In situ nanomechanics of GaN nanowires. *Nano Lett.* **11** 1618–22

[25] Plimpton S 1995 Fast Parallel Algorithms for Short – Range Molecular Dynamics *J. Comput. Phys.* **117** 1–19

[26] Zapol P, Pandey R and Gale J D 1997 An interatomic potential study of the properties of gallium nitride *J. Phys. Condens. Matter* **9** 9517–25

[27] Fennell C J and Gezelter J D 2006 Is the Ewald summation still necessary? Pairwise alternatives to the accepted standard for long-range electrostatics *J. Chem. Phys.* **124** 1–12

[28] Kioseoglou J, Polatoglou H M, Lymperakis L, Nouet G and Komninou P 2003 A modified empirical potential for energetic calculations of planar defects in GaN *Comput. Mater. Sci.* **27** 43–9

[29] Wang Z, Zu X, Yang L, Gao F and Weber W J 2008 Orientation and temperature dependence of the tensile behavior of GaN nanowires: An atomistic study *J. Mater. Sci. Mater. Electron.* **19** 863–7

[30] Jaffe J E, Pandey R and Zapol P 1996 Ab initio prediction of GaN (10 1^{-} 0) and (110) anomalous surface relaxation *Phys. Rev. B* **53** R4209

[31] Zhou L G and Huang H 2004 Are surfaces elastically softer or stiffer? *Appl. Phys. Lett.* **84** 1940–2

[32] Thompson A P, Plimpton S J and Mattson W 2009 General formulation of pressure and stress tensor for arbitrary many-body interaction potentials under periodic boundary conditions *J. Chem. Phys.* **131** 1–6

[33] Stukowski A 2009 Visualization and analysis of atomistic simulation data with OVITO–the Open Visualization Tool *Model. Simul. Mater. Sci. Eng.* **18** 5012

[34] Chen C, Meng F and Song J 2015 Core structures analyses of (a+c)-edge dislocations in wurtzite GaN through atomistic simulations and Peierls-Nabarro model *J. Appl. Phys.* **117** 194301

[35] Kang K and Cai W 2007 Brittle and ductile fracture of semiconductor nanowires - molecular dynamics simulations *Philos. Mag.* **87** 2169–89

[36] Kang K and Cai W 2010 Size and temperature effects on the fracture mechanisms of silicon nanowires : Molecular dynamics simulations *Int. J. Plast.* **26** 1387–401

[37] Leach B A M, Mcdowell M and Gall K 2007 Deformation of Top-Down and Bottom-Up Silver Nanowires *Adv. Funct. Mater.* **17** 43–53

[38] Ji C and Park H S 2007 The coupled effects of geometry and surface orientation on the mechanical properties of metal nanowires *Nanotechnology* **18** 305704

[39] Androussi Y, Vanderschaeve G, Lefebvre A and Vanderschaeve G 1989 Slip and twinning in high-stress-deformed GaAs and the influence of doping *Philos. Mag. A* **59** 1189–204

[40] Pirouz P and Hazzledine P M 1991 Cross-Slip and Twinning in Semiconductors *Scr. Metall. Mater.* **25** 1167–72

[41] Lloyd S J, Castellero A, Giuliani F, Long Y, McLaughlin K K, Molina-Aldareguia J M, Stelmashenko N A, Vandeperre L J and Clegg W J 2005 Observations of nanoindents via cross-sectional transmission electron microscopy: a survey of deformation mechanisms *Proc. R. Soc. A* **461** 2521–43

[42] Michler J, Wasmer K, Meier S, Östlund F and Leifer K 2007 Plastic deformation of gallium arsenide micropillars under uniaxial compression at room temperature Plastic deformation of gallium arsenide micropillars under uniaxial *Appl. Phys. Lett.* **90** 43123

[43] Brochard S and Godet J 2011 Unexpected slip mechanism induced by the reduced dimensions in silicon nanostructures : Atomistic study *Acta Mater.* **59** 7464–72

[44] Zhang Y, Han X, Zheng K, Zhang Z, Zhang X, Fu J, Ji Y, Hao Y, Guo X and Wang Z 2007 Direct observation of super-plasticity of beta-SiC nanowires at low temperature *Adv. Funct. Mater.* **17** 3435–40

[45] Han X, Zheng K, Zhang Y, Zhang X, Zhang Z and Wang Z L 2007 Low-temperature in situ large-strain plasticity of silicon nanowires *Adv. Mater.* **19** 2112–8

[46] Wang S, Shan Z and Huang H 2017 The Mechanical Properties of Nanowires *Adv. Sci.* **4** 1600332

[47] Wang R J, Wang C Y and Feng Y T 2017 International Journal of Mechanical Sciences

Effective geometric size and bond-loss effect in nanoelasticity of GaN nanowires *Int. J. Mech. Sci.* **130** 267–73

[48] Agrawal R, Peng B and Espinosa H D 2009 Experimental-computational investigation of ZnO nanowires strength and fracture. *Nano Lett.* **9** 4177–83

[49] Zhang L and Huang H 2006 Young's moduli of ZnO nanoplates: Ab initio determinations *Appl. Phys. Lett.* **89** 9–12

[50] Liang H, Upmanyu M and Huang H 2005 Size-dependent elasticity of nanowires: Nonlinear effects *Phys. Rev. B* **71** 1–4